

Differential imaging in coherent anti-Stokes Raman scattering microscopy with Laguerre-Gaussian excitation beams

Cheng Liu and Dug Young Kim

Department of Information and Communications, Gwangju Institute of Science and Technology
Buk-gu, Gwangju, Republic of Korea 500-712

Liucheng@gist.ac.kr

Abstract: We propose a new differential imaging technique to visualize the fine structures and the edges of a sample in coherent anti-Stokes Raman Scattering (CARS) microscopy. Both the pump and Stokes excitation fields are modulated simultaneously with a spiral phase mask which transforms them from Gaussian modes into Laguerre-Gaussian modes of LG01 for CARS excitation. With an accurate three dimensional finite-difference time-domain (FDTD) method, the intensity and phase distributions of focused input fields, the scattering pattern of generated CARS signal as well as the formation of differential images are studied detailedly, and by simulating the sensitivity range and reliability of this method, we have verified that it is much suitable for visualizing structures with a scale comparable to the excitation wavelength and has higher reliability in retrieving chemical structural information of the sample compared to common CARS microscopy.

©2007 Optical Society of America

OCIS codes: (290.5860) Scattering Raman; (300.6230) Spectroscopy, Coherent anti-Stokes Raman scattering; (180.1790) Confocal microscopy; (330.6130) Spatial resolution

References:

1. R. J.H. Clark and R. E. Hester, *Advances in Nonlinear Spectroscopy*, (Wiley, New York, 1988) 15.
2. P.D. Maker and R.W. Terhune, "Study of optical effects due to an induced polarization third order in the electric field strength," *Phys. Rev.* **137**, A801-A818 (1965).
3. Y. R. Shen, *The principles of nonlinear optics* (Wiley, New York, 1984).
4. J. X. Cheng and X. S. Xie, "Coherent Anti-Stokes Scattering Microscopy: Instrumentation, Theory, and Application," *J. Phys. Chem. B.* **108**, 827-840 (2004).
5. J. X. Cheng, A. Volkmer, and X. S. Xie, "Theoretical and experimental characterization of Coherent anti-Stokes Raman scattering microscopy," *J. Opt. Soc. Am. B.* **19**, 1363-1375 (2002).
6. H. Wang, Y. Fu, P. Zickmund, R. Shi, and J. X. Cheng, "Coherent Anti-Stokes Raman Scattering Imaging of Axonal Myelin in Live Spinal Tissues," *Biophysical Journal* **89**, 581-591 (2005).
7. E. O. Potma, C. L. Evans, and X. S. Xie, "Heterodyne Coherent anti-Stokes Raman scattering (CARS) imaging," *Opt. Lett.* **31**, 241-243 (2006).
8. J. P. Ogilvie, E. Beaupire, A. Alexandrou, and M. Joffre, "Fourier-transform coherent anti-Stokes Raman scattering microscopy," *Opt. Lett.* **31**, 480-482 (2006).
9. D. Oron, N. Dudovich, and Y. Silberberg, "Single-Pulse Phase-contrast nonlinear Raman Spectroscopy," *Phys. Rev. Lett.* **89**, 273001-273004 (2002).
10. E. R. Andresen, H. N. Paulsen, V. Birkedal "Broadband multiplex coherent anti-Stokes Raman scattering microscopy employing photonic-crystal fibers," *J. Opt. Am. B.* **22**, 1934-1938 (2005).
11. J. X. Cheng and X. S. Xie, "Green's function formulation for third-harmonic generation microscopy," *J. Opt. Soc. Am. B.* **19**, 1604-1610 (2002).
12. V. V. Krishnamachari, E. O. Potma, "Focus-engineered coherent anti-Stokes Raman scattering microscopy: a numerical investigation," *J. Opt. Soc. Am. A* **24**, 1138-1147 (2007).
13. K. S. Yee. "Numerical solution of initial boundary value problem involving Maxwell equations in isotropic media," *IEEE Trans. Antennas Propagat.* **14**, 302-307 (1966).
14. A. Taflov, *Computational Electrodynamics: The Finite-Difference Time-Domain Method* (Artech House, Boston, 1995).

15. R. W. Boyd, *Nonlinear Optics* (Academic, Boston, Mass., 1992).
 16. S. Mukamel, *Principles of Nonlinear Optical Spectroscopy* (Oxford U. Press New York, 1995).
 17. M.W. Beijersbergen, R.P.C. Coewinkel, M. Kristensen, J.P. Woerdman, "Helical-wavefront laser beams produced with a spiral phase plate," *Opt. Comm.* **112**, 321-327 (1994)
 18. K. Crabtree, J. A. Davis, and I. Moreno, "Optical processing with vortex-producing lenses," *Appl. Opt.* **43**, 1360-1367(2004).
 19. K. Takeda, Y. Ito and C. Munakata, "Simultaneous measurement of size and refractive index of a fine particle in flowing liquid," *Meas. Sci. Technol.* **3**, 27-32 (1992).
 20. M. Hashimoto and T. Araki, "Three-dimensional transfer functions of coherent anti-Stokes Raman scattering microscopy," *J. Opt. Soc. Am. A* **18**,771-776 (2001).
 21. L. Cheng , H. Zhiwei , L. Fake , Z. Wei , H. W. Dietmar, S. Colin "Near-field effects on coherent anti-Stokes Raman scattering microscopy imaging," *Opt. Express* **15**, 4118-4131(2007).
-

1. Introduction

Coherent anti-Stokes Raman Scattering (CARS) is a four-wave-mixing process involving in interactions between a pump beam of frequency ω_p , a Stokes beam of frequency ω_s , and a CARS signal at the anti-Stokes frequency of $\omega_{as}=2\omega_p-\omega_s$ generated in the phase matching direction [1]. The vibrational contrast in CARS microscopy is created when the frequency difference $\omega_p-\omega_s$ between the pump and the Stokes beams is tuned to be resonant with a Raman-active molecular vibration of samples. Recently, CARS technique has received great interest in imaging live cells [2-10], owing to its outstanding abilities in providing both the biochemical compositions and bio-molecular structural information about bio-samples in aqueous solutions without fluorescence probes. It also provides high sensitivity as well as intrinsic three-dimensional optical sectioning ability with high spatial and spectral resolutions. As CARS is a coherent process, far-field intensity pattern of a generated CARS signal is always under the influence of interference between lights emitted from different points in a focal volume. Since constructive and destructive interferences are dominant at forward and backward directions respectively, signal detected in the forward direction can be hundreds time stronger than that in the backward direction [4]. Though the intensity of the signal in forward direction is taken in most of experiments, it lacks the ability to reveal the fine structure of a specimen, because strong un-resonant back ground coming from water included in a bio-sample contributes most of its emission in the forward direction and make the fine structures in a detected image very dim [4, 5, 11]. On the other hand, the fine structure inside the sample can radiate its signal almost equally in both forward and backward directions, thus the image detected in the epi-direction can retrieve the fine structure of a sample much better than that of forward direction. However, because the intensity of the epi-direction is so weak and almost comparable to the noise level of a common detector (such as photodiode), it is not easy to obtain a satisfying image with epi-detection either. Thus finding a method to generate images with both high resolution and satisfying intensity would be very attractive for CARS microscopy.

It was recently shown by numerical simulation that background CARS signals from a uniform specimen can be suppressed by utilizing a Gaussian beam for pump light and various Hermite-Gaussian beams for Stokes light [12]. By using a 2-dimensional model with analytic functions, Krishnamachari et al. have shown that this focus-engineered CARS microscopy technique can enhance the edges of a CARS microscopy image significantly. Even though it was proved that sharp edges in CARS microscopy images can be efficiently enhanced by using this kind of excitation, there are some difficulties in applying this method in practical CARS microscopy because a focused Gaussian beam and a higher order Hermite-Gaussian beam are remarkably different not only in phase distribution but also in intensity distribution. When a Gaussian and an LG01 Laguerre-Gaussian beams are used as the pump and the Stokes lights of CARS microscopy respectively, their intensity peaks don't overlap spatially, and the intensity of generated CARS signal will be very weak; a focused Laguerre-Gaussian beam of LG01 mode has a hollow focal spot, and its intensity is almost zero at the center of a focal volume, while the intensity of a Gaussian beam is maximum at the center of a focal volume.

Another important problem in CARS microscopy is how to identify a small object or a scattering point whose CARS signal is weaker than that of a background material. For a small object whose size is smaller than the focal volume of a focused beam in confocal CARS microscopy, the phase and the intensity distribution of generated CARS signal would be too much complicated to be described with analytical functions in numerical simulation. Due to difficulties in considering the effects of scattering, index-mismatch, and diffraction in numerical simulation, the advantages of the focus-engineered CARS microscopy on visualizing a small object with a very weak CARS signal are not taken into consideration in previously reported literatures. In this paper we have modified the focus-engineered CARS microscopy initially proposed by Krishnamachari et al. [12]. Here, we have used Laguerre-Gaussian beams for both pump and Stokes lights to enhance overlap integral between the pump and the Stokes lights. A confocal system is employed for signal detection. We have adapted three dimensional finite-difference time-domain (FDTD) method [13, 14] in combination with nonlinear optics formulas in order to investigate scattering, index-mismatch, and diffraction effects in our modified focus-engineered CARS microscopy. Since FDTD is an iterative method to solve the Maxwell's equation, there is no assumption or approximation needed; the index-mismatch, scattering, phase matching, near-field effects, and polarization effects, which are difficult to be studied with analytical methods, are all considered in the calculation automatically. Thus the numerical results of this paper can be comparable to the practical experiments.

Our numerical results show that the intensity and the phase of CARS signal generated in a uniform specimen have radially symmetric and anti-symmetric distributions respectively. This results in a shape of bugle for far-field CARS radiation pattern. When this kind of scattering pattern is collected with a confocal system, detected optical power is negligible compared to the actual optical power of generated CARS signal. When there is a tiny scatterer such as a polystyrene bead whose diameter is comparable to the wavelength of a pump or a Stokes beam in the focal volume, the distribution of the excitation fields and the induced nonlinear polarization are remarkably different from those of uniform specimen due to the combining effect of index-mismatch, scattering, and diffraction. We have shown that the measured optical power of generated CARS signal from the scatterer can be hundreds times stronger than that of a uniform specimen when this kind of scattering pattern is collected by a confocal system. Thus our proposed excitation technique using a higher order Laguerre-Gaussian mode combined with a confocal detection scheme can enhance the fine structure of the specimen, and background CARS signal can be efficiently suppressed. This is a kind of a differential imaging technique visualizing fine structures in a specimen. By calculating the CARS intensity of scatterers with various diameter sizes, it is also shown that the sensitivity of this method is maximized when the size of the structure is compatible to the spot size of a focused beam. As CARS signal from a fine scatterer becomes dominant in the detected image in our proposed technique the ability of CARS microscopy in retrieving the chemical structural information of a sample is enhanced compared to that of common CARS microscopy.

2. Geometry and parameters of the simulated setup

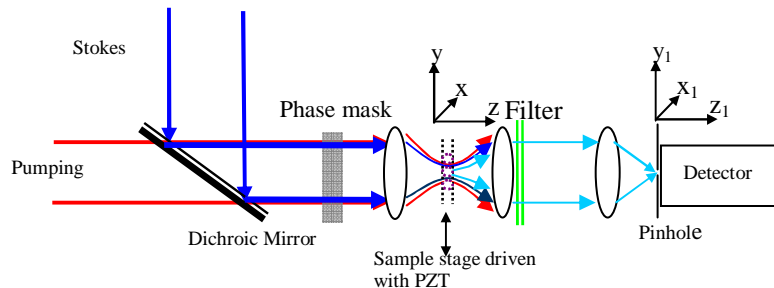


Fig.1. Confocal CARS microscopy setup for numerical simulation.

We have considered an experimental setup schematically shown in Fig. 1, where both pumping beam at 750 nm wavelength and Stokes beam at 852 nm wavelength are expanded into plane waves and combined together with diachronic mirror first and is modulated by one spiral phase modulator. Then lights from the phase modulator are focused onto a specimen by a microscope objective lens with a numerical aperture (N.A.) of 0.75, forming collinear excitation geometry. The generated CARS signal is collected by a confocal system through a pinhole. The sample is fixed on a translation stage driven by a PZT. The sample used in our numerical simulation is polystyrene beads immersed in water

The generation and propagation of a CARS field in a homogeneous and isotropic medium are governed by the wave equation [15, 16].

$$\nabla \times \nabla \times \mathbf{E}(\mathbf{r}, t) + \frac{n^2}{c^2} \frac{\partial^2 \mathbf{E}(\mathbf{r}, t)}{\partial t^2} = -\frac{4\pi}{c^2} \frac{\partial^2 \mathbf{P}^{(3)}(\mathbf{r}, t)}{\partial t^2} \quad (1)$$

where $\mathbf{P}^{(3)}(\mathbf{r}, t)$, $\mathbf{E}(\mathbf{r}, t)$ are third-order nonlinear polarization and generated electric field, respectively, n is the refractive index of a medium, and c is the speed of light in vacuum. The third-order polarization at the anti-Stokes frequency of $\omega_{as} = 2\omega_p - \omega_s$ can be written as

$$P_i^{(3)}(\mathbf{r}, \omega_{as}, t) = 3 \sum_{jkl} \chi_{ijkl}^{(3)} E_j^P(\mathbf{r}, \omega_p, t) E_k^P(\mathbf{r}, \omega_p, t) E_l^{S*}(\mathbf{r}, \omega_s, t) \quad (2)$$

where $\chi_{ijkl}^{(3)}$ is the third-order nonlinear coefficient of a medium, and $E_j^P(\mathbf{r}, \omega_p, t)$, $E_k^P(\mathbf{r}, \omega_p, t)$ and $E_l^{S*}(\mathbf{r}, \omega_s, t)$ are the time-dependant amplitudes of pumping and Stokes electric fields in j , k , and l directions, respectively. If the distributions of the pumping and the Stokes electric fields as well as the third-order nonlinear coefficient are known, the third-order nonlinear polarization at any direction can be determined by Eq. (2), and then the generated electric field of a CARS signal can be obtained by solving Eq.(1).

3. Finite-difference time-domain (FDTD) method for simulations

In theory we can obtain a generated CARS signal for any specimen with Eq.(1) and Eq.(2), however, it is difficult to explicitly describe the excitation light fields and the induced nonlinear polarization for most of practical experiments with analytical functions due to complexity in determining boundary conditions, except for in some very simple cases. In order to resolve this problem, we have used an FDTD method to simulate the excitation fields, the induced nonlinear polarization, and the generated CARS field.

When there is no free electric charge and current source in the medium of interest, the Maxwell equations can be written as [13, 14]

$$\begin{cases} \nabla \times \mathbf{H} = \frac{\partial \mathbf{D}}{\partial t} \\ \nabla \times \mathbf{E} = -\frac{\partial \mathbf{B}}{\partial t} \end{cases} \quad (3)$$

Where \mathbf{H} , \mathbf{D} , \mathbf{E} , and \mathbf{B} , stand for magnetic field, electric displacement, electric field, and magnetic flux density, respectively. In FDTD simulations, Eq. (3) is discretized with standard staggered grids in temporal and spatial domains. The discretized equations for electric fields in the FDTD simulator for 3-D coordinates are as follows:

immersion objective lens with a numerical aperture of 0.75. Both the pumping and the Stokes beams are assumed to be ideal Gaussian beam before they reach the spatial phase modulator, which has a phase distribution of $\exp(i\varphi)$, where the φ is the polar angle in a plan transverse to the light propagation direction [17, 18]. If the incident light is assumed to be polarized in the x -direction and the index of the water is assumed to be 1.33, we can simulate the distribution of its focal field with an FDTD method. Fig. 2(a), Fig.2 (b), and Fig.2 (c) show the simulated amplitudes and the related phase of the focused pumping field along x , y , and z directions, respectively on the focal plan of the objective lens.

We can find in Fig.2 that, the distribution of the focal field is remarkably different from that of common Gaussian beam, and each components of the focal field is radially symmetric in intensity and asymmetric in phase. A hollow focal field is formed by the x -component with zero amplitude at the center. The amplitude of the x -component is about 3-times stronger than that of y -component. CARS generation is a third order nonlinear process. According to Eq. (2) the intensity of the induced the nonlinear polarization along the x -axis is at least $3^6=279$ times stronger than those along the y or z axes. Therefore, we may only consider the CARS signal polarized along the x -axis for simplicity in calculation. The Stokes beam shows a similar distribution as those given in Fig. 2, and those results are not shown here.

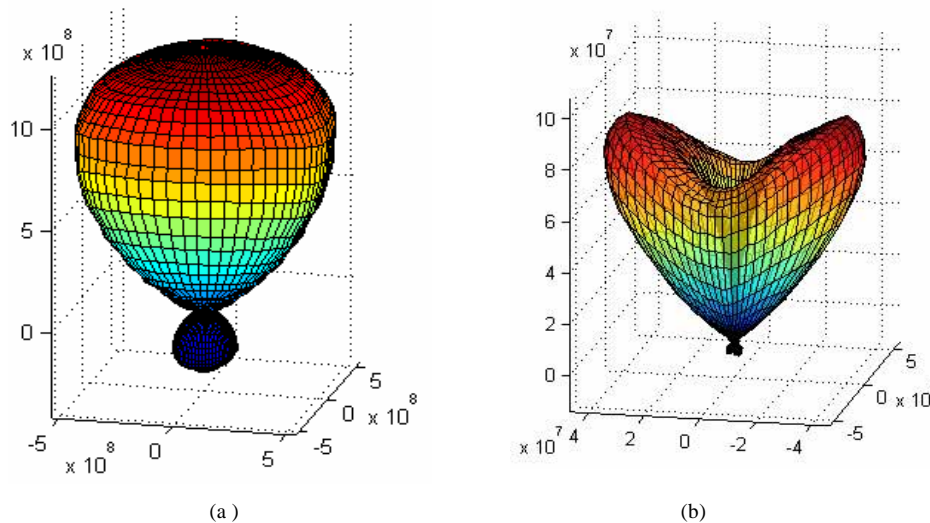


Fig. 3. Calculated far-field CARS radiation patterns with (a) Gaussian and (b) spiral phase excitation beams.

According to Eq. (2), the induced CARS polarization by excitation in Fig. 2 also has symmetric intensity and asymmetric phase on the focal plan, thus the CARS signals from different points in the focal plan will have destructive interferences in the forward direction, resulting in a very weak generated CARS signal along the forward direction. For practical CARS experiments for imaging bio samples, this means an efficient suppression for non-resonant background CARS signals from water along the forward direction. To verify this expectation, we have simulated the scattering pattern of water under the illumination of a focused spiral phase beam. In the simulation we firstly calculate the distribution of the focus of the pumping and Stokes beams with FDTD and, then the induced nonlinear CARS polarization is determined with Eq.(2). The propagation of the generated CARS signal is simulated with an FDTD method by considering the CARS nonlinear polarization. The nonlinear coefficient of water is assumed to be 0.6 in the simulation [1]. Fig. 3 shows simulated far-field CARS radiation pattern of uniform water. Fig. 3(a) is scattering pattern under excitation by a Gaussian beams, and Fig. 3(b) is the scattering pattern under excitation of a spiral phase beam as an approximated Laguerre-Gaussian beam of LG01. For the CARS

signal with Gaussian excitation beams the maximal intensity is along the propagation axis of the beam, while the CARS signal generated with LG01 Laguerre-Gaussian excitation beams shows almost zero intensity along the propagation axis direction.

4.2 Excitation field and CARS scattering pattern of tiny scatterer

The sizes of organelles in bio-samples are normally less than 1 μm and comparable to the wavelength used in CARS microscopy. Thus generated CARS signal as well as both of pump and Stokes lights will be remarkable scattered when some organelles are included inside the focal volume of a confocal CARS setup. To investigate the effects of the spiral phase excitation beam on CARS signal generation and propagation around these organelles, a polystyrene bead with a diameter of 800nm assumed to be located inside the focal spot, and the distribution of the excitation field and the scattering of the induced CARS signal are studied with an FDTD method. The position of the polystyrene bead is indicated in Fig. 4 with a circle. In the calculation, the refractive indices of the polystyrene bead and surrounding water are assumed to be 1.56 and 1.33, respectively.

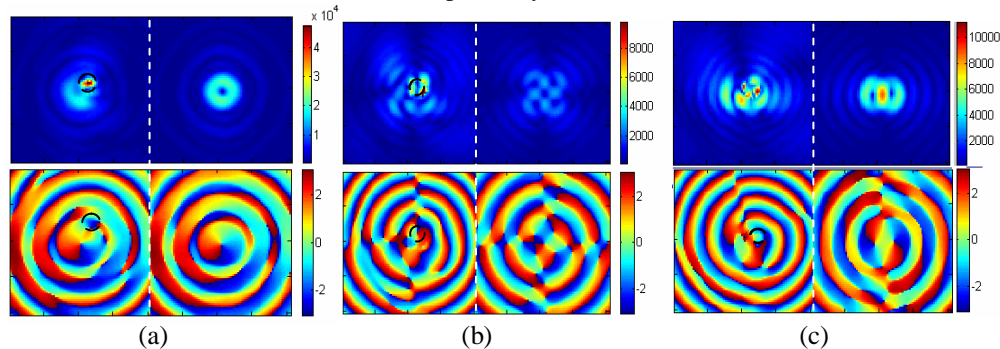


Fig. 4. Simulated amplitudes (upper figures) and phases (lower figures) of a focused spiral phase fields with a polystyrene bead represented with a circle in each left side figure. Right side figures are without polystyrene bead

Figure 4(a), Fig. 4(b), and Fig. 4(c) show the distributions of x-, y-, and z- components of the focused pumping field, respectively at the beam waist position represented as x-y plan in Fig. 1. The corresponding distributions without a polystyrene bead are shown at the right side of each figure. It can be found in Fig. 4 that the intensity distribution around the scatterer is remarkably different from that of a uniform material. Symmetric distributions in amplitude plots are quite much broken. This can be explained as the results of the index-mismatch at the water/bead interface and related scattering, which lead to the redistribution of the field inside the focal volume. However, there are almost no remarkable changes in the phase distributions; both phase plots are roughly same and asymmetric with respect to the center regardless of the existence of the polystyrene bead.

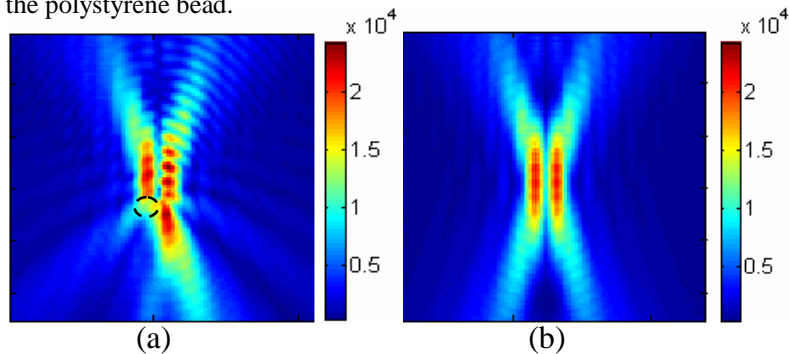


Fig. 5. Scattered amplitude distribution of focused pump light on the x-z plan near the beam waist with a polystyrene bead (a) and without a bead (b).

To clearly show the effects of the scattering of the polystyrene bead on the redistribution of the excitation field, the intensity distribution on the x - z plan near the beam waist of the focused beam is shown in Fig. 5. Fig. 5(a) and Fig. 5(b) represent the intensity of the focal fields with and without a polystyrene bead, respectively. Obvious interference fringes can be found in the upper space of the focal volume shown in Fig. 5(a), which is the evidence of the strong reflection at the water/bead interface. On the other hand, due to diffraction, the light transmitted through the poly-bead becomes dispersed and only one lobe is remained. The same phenomenon can be also found in the focused Stokes beam.

After the pumping and Stokes field are both determined, the induced CARS polarization can be directly obtained with Eq. (2), and the scattering and propagation of the CARS signal are simulated with an FDTD method by putting the induced nonlinear polarization $P_i^{(3)}(r, \omega_{as}, t)$ into Eq. (1). Fig. 6(a) is a calculated scattering patterning, which is intensity distribution on a sphere centered on the geometric focal point with a diameter of 200 μm . The position of the poly-bead is same as that of Fig. 4 or Fig. 5. We have assumed the nonlinear coefficient and the refractive index of the poly-bead to be $0.6(1+0.5i)$ and 1.56, respectively [1, 19]. As can be seen in Fig. 5(a) the pump beam is very much reflected by the poly bead located at one of the two peaks of the incoming Laguerre-Gaussian LG01 mode. As a direct result of the redistribution of the excitation field, the scattering patterning in Fig. 6(a) is almost same as one half of Fig. 3(b). Fig. 6 (b) is the generated CARS field distribution (x -component) exactly behind the poly-bead, where we can find that the phase distribution is very similar to that of common divergent light from a point source. This means that the scattering patterning in Fig. 6 has roughly equal phase at different angle. When it is collected by a confocal system, the signal scattered in different angle will instructively interfere with each other along the propagation axis resulting in a very strong detected signal through a pinhole for a given confocal detection system.

We have also found that the back scattering shown in Fig. 6 is obviously stronger than that shown in Fig. 3(b), this could be partially explained as the result of the reflection shown in Fig. 5. Reflected excitation lights from the interface of water and the poly-bead sample generate non-resonant CARS signal propagation through water, which makes enhanced CARS signal in the epi-direction.

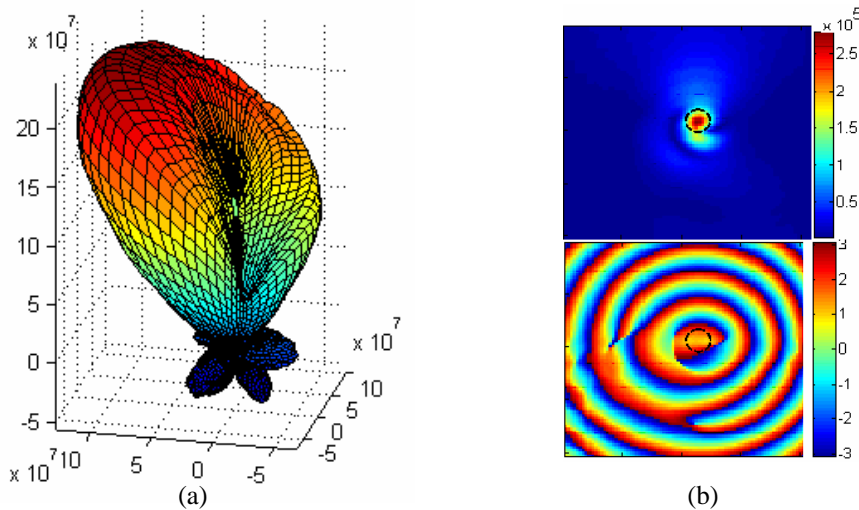


Fig. 6. Scattering pattern for the generated CARS signal (a) and x -component of generated CARS electric field just after the poly-bead.

5. Differential image with spiral phase excitation beams

It is well known that the amplitude point spread function of a confocal system is the product of the point spread functions of the illuminating and collection objectives. For CARS microscopy with a confocal setup shown in Fig. 1 the detected signal can be obtained by convolving the induced nonlinear polarization on the focal plan with the point spread function of the collecting lens and calculating its integration [20].

$$I_{Det} = \int_{-\Delta y/2}^{\Delta y/2} \int_{-\Delta x/2}^{\Delta x/2} \left| \int_{-\infty}^{+\infty} \int_{-\infty}^{+\infty} P^{(3)}(x, y, \omega_{as}) g(x_1 - x, y_1 - y) dx dy \right|^2 dx_1 dy_1 \quad (5)$$

where, $g(x_1, y_1)$ is the amplitude point spread function of the collecting objective lens, which always is circularly symmetric and can be simplified with a two-dimensional Bessel function. $P^{(3)}(x, y, \omega_{as})$ is the induced nonlinear CARS polarization in the focal plan. Δx and Δy are the sizes of the detecting pinhole in x- and y- directions respectively. For common CARS system with Gaussian excitation beams, $P^{(3)}(x, y, \omega_{as})$ is circularly symmetric in a uniform specimen. Then the detected signal determined by Eq. (5) will be relatively very strong, because Eq. (5) essentially indicates constructive interferences between induced nonlinear polarizations from different points on the focal plan. For our case, both the pumping and Stokes lights are LG01 Laguerre-Gaussian beams, and the induced nonlinear CARS polarization $P^{(3)}(x, y, \omega_{as})$ has a radially anti-symmetric phase distribution and a symmetric intensity distribution for a uniform specimen. Then Eq. (5) indicates an overall cancellation in the detected CARS signal due to destructive interferences of $P^{(3)}(x, y, \omega_{as})$ on the focal plan, resulting in a very weak detected signal of I_{dec} . When a tiny scatterer is included in the focal volume, the excitation and induced CARS fields inside the focal volume will be redistributed due to the index-mismatch, scattering, diffraction, and near-field effects. The symmetry in the intensity and the anti-symmetry in the phase of generated nonlinear polarization $P^{(3)}(x, y, \omega_{as})$ would disappear in this case. Thus there should be an increase in the intensity of the CARS signal I_{dec} determined by Eq. (5). This suggests that the CARS microscopy has the ability to suppress the background from uniform bulk material and highlight the fine structures of a specimen by using LG01 Laguerre-Gaussian beams for excitation and a confocal system for signal detection. For imaging a bio-sample, this means that the strong non-resonant background from the bulk scattering of the water could be effectively eliminated, and the fine structures dimmed by the background can be highlighted accordingly. Therefore, the capability of the CARS microscopy on identifying fine structures is improved in our scheme.

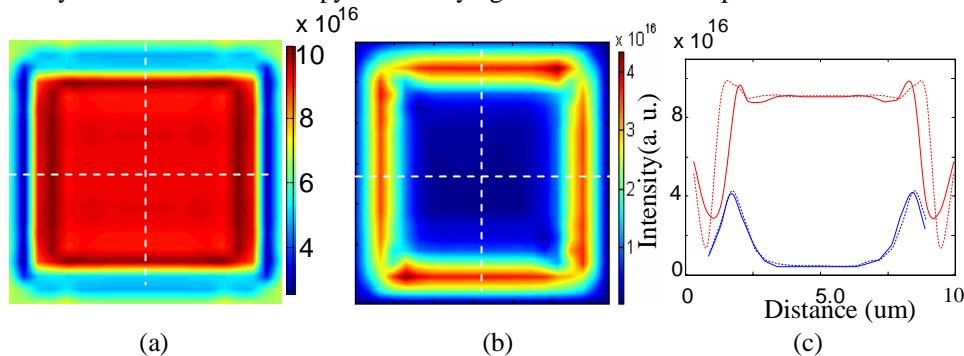


Fig. 7. Simulated CARS image for a 7 μm polystyrene square with standard Gaussian excitation beams (a), with LG01 Laguerre-Gaussian beams (b). Line-scan intensity profiles along the crossed lines in CARS images (c).

In order to verify this differential imaging capability of our proposed method, we have considered the imaging of a polystyrene slice emerged in water with our method. The

dimensions of a polystyrene square sample are $7\ \mu\text{m}$ in length and width with $3\ \mu\text{m}$ in thickness. The numerical aperture of the illuminating and the collector lenses are both assumed to be 0.75. The nonlinear coefficient of the water and the polystyrene are assumed to be 0.6 and $0.6(1+0.5i)$, respectively. The refractive index of water is assumed to be 1.33 while that of the polystyrene is assumed to be 1.56. Fig. 7 (a) shows the image under common Gaussian excitation beams. There is a ringing effect around the border of the polystyrene square, and its degree is much larger in vertical edges at the right and left sides of the square than horizontal edges at upper and lower sides. This asymmetric intensity ringing along the horizontal and vertical directions can be explained with the combining effect of the diffraction and the polarization of input fields. Due to the scattering of input fields at the boundary of the sample, the intensities of exciting fields decrease near the boundary. Hence the generated CARS signal decreases there as well, and this generates a dark ring around the edge of a specimen. We have assumed linearly polarized input fields in our simulation along the vertical direction. On the upper and lower horizontal boundaries in Fig. 7(a) the continuity condition of the electric displacement D leads to a larger intensity of electric field [21] in water on the boundary. Therefore, the decrease of the exciting fields on the horizontal boundaries is not as large as that of vertical ones. This is the reason why the magnitude of dark ring in CARS image becomes dim at the upper and the lower sides in Fig. 7(a). Line-scan CARS intensity profiles along horizontal and vertical dotted lines in Fig. 7(a) are displayed in Fig. 7(c). Red and blue lines represent intensity profiles in the images with normal Gaussian (Fig. 7(a)) and Laguerre-Gaussian excitation beams (Fig. 7(b)), respectively. Line-scan profiles with dotted lines represent intensity profiles along the horizontal direction, while the solid lines represent intensity profiles along the vertical direction. The contrast of the CARS image is less than 2 in Fig. 7(a); the image intensity of the polystyrene slice is 9×10^6 , and the intensity of the water is about 6.5×10^6 . In Fig. 7(b) the edges of the polystyrene slice are remarkably highlighted while uniform CARS intensity inside the square of the polystyrene sample shown in Fig. 7(a) is quite much depressed. The contrast of the image is about 50 in this case; the peak intensity of the polystyrene slice edge is about 3.7×10^6 , and the background intensity is about 7.4×10^4 . From the analysis in section 2.4 we know that the edge highlighting in Fig. 7 (b) originates from the asymmetry of the optical parameters at the boundary, and it includes the effects of both the index-mismatch and the nonlinear coefficient difference between the surrounding water and the polystyrene sample. Thus our edge detection scheme in CARS microscopy is due to the combined effect of both linear and the nonlinear refractive index differences between two media at boundaries. It has been shown in Ref [12] that generated nonlinear optical signal at an edge is still very remarkable with a Laguerre-Gaussian beam even when the refractive indices of two media at the boundary are same.

Above results indicate the possibility of differential imaging in CARS microscopy highlighting the edges of a specimen with LG01 Laguerre-Gaussian excitation beams. However, in practical CARS microscopy applications with bio samples there is a need to identify microscopic structures with different sizes. To investigate the capability of identifying small objects using our proposed method, we have simulated the CARS imaging of tiny scatterers with various sizes located inside the focal volume of our setup. Fig. 8(a) shows CARS signal intensity for polystyrene disks with a thickness of 200 nm and various radius from 100 nm to 1500 nm. The center of the scatterer is assumed to be located at the position of the intensity peak of the focused LG01 Laguerre-Gaussian beam. A curve marked with empty circles is the total CARS signal intensity, which includes the signal from a scatterer and that from surrounding water. When a scatterer with a size comparable to the excitation wavelength is located inside the focal spot the hollow scattering pattern of generated CARS signal toward the propagation direction shown in Fig. 3(b) will be changed to the pattern shown in Fig. 6(a). This change is not only because of the asymmetric distribution of a sample but also due to the asymmetric distribution of water inside the focal volume of the incoming excitation beams. The contributed CARS signal from the asymmetric

water distribution associated with the asymmetric location of a scatterer inside the focal volume of the excitation beams can not be totally eliminated like the case for CARS signal from uniform bulk water.

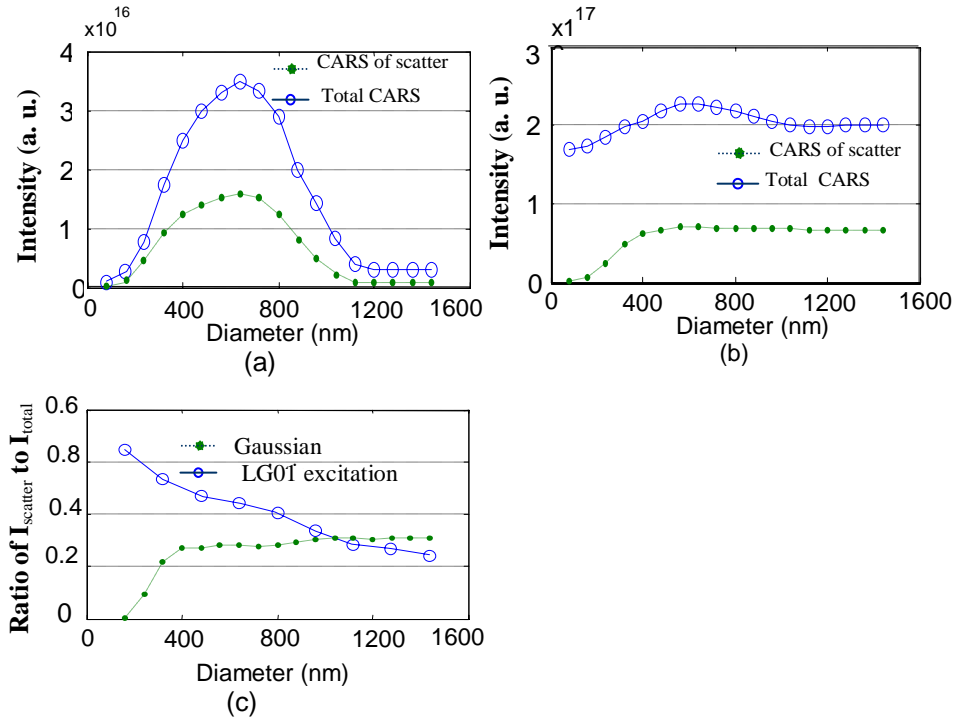


Fig. 8. CARS signal intensities with LG01 Laguerre-Gaussian excitation beams (a), and with Gaussian excitation beams (b). The ratio of CARS signal only from a scatterer with respect to the total CARS signal for both excitation cases are calculated and plotted in (c).

Since the CARS signal from water is purely non-resonant and carries no chemical information about a specimen, it is very important for us to know how much CARS signal from the scatterer is included in the image. For this purpose, we have calculated the CARS signal that comes only from the scatterer. When the size of the scatterer increases from zero, the CARS signal from the scatterer as well as that from water increase simultaneously at the beginning. Both of them reaches the maximum values when the radius of the scatterer is about 700 nm and then, then the intensities decrease fast with the increase of the scatterer size. The maximum CARS intensity is obtained when the size of the scatterer becomes about the size of one of the double peaks of the focused LG01 Laguerre-Gaussian beam on the focal plan. When the size of the scatterer is comparable to the size of one of the double peaks of the focused LG01 Laguerre-Gaussian beam or the excitation laser wavelength used, the anti-symmetric phase distribution of LG01 is mostly distorted by the effects of diffraction and scattering, and thus the detected signal becomes strongest. When the scatterer is small enough the focal field keeps an asymmetric phase distribution due to the very weak influence of the tinny scatterer, and a low intensity is obtained by confocal detection system as a result of the destructive interference. On the contrary, when the scatterer is so large that it can cover the total focal spot of the focused LG01 Laguerre-Gaussian beam, the scatterer is essentially regarded as bulk material, and the detected signal becomes weak.

Fig. 8(b) shows the simulated CARS signal with common Gaussian excitation beams. Total CARS signal intensity including the signal from a scatterer and that from surrounding water is shown with a curve with empty circles. A curve with small solid dots is the CARS signal that originates only from the scatterer. Again, the CARS signal from the scatterers only

contributes part of the total detected CARS signal. It shows that the CARS intensity with common Gaussian beams excitation is almost seven times stronger than that with Laguerre-Gaussian excitation beams. However generated CARS signal intensity doesn't change much with the variation of the size of the scatterer. For practical experiment this indicates low image contrast for small sample structures.

The ratio of the signal from the scatterers I_{scatter} to that of the total signal I_{total} is given in Fig. 8(c). A curve marked with hollow circles corresponds to the method with Laguerre-Gaussian excitation beams, and another one with small solid dots corresponds to the case with common Gaussian excitation beams. For the case of Laguerre-Gaussian beams, the CARS signal from the scatterers is dominant when the size of the scatterer is small, and the ratio of I_{scatter} to I_{total} decreases with the increase of scatterer size. On the contrary, for the case with common Gaussian excitation beams the ratio of I_{scatter} to I_{total} increases with the scatterer size and approaches a constant of 0.3 when the scatterer size becomes larger than 400 nm. It shows that the I_{scatter} to I_{total} ratio with Laguerre-Gaussian excitation beams is larger than that of common Gaussian excitation beams when the size a scatterer ranges from 400 nm to 1000 nm, which corresponds to the case of enhanced signal intensity with Laguerre-Gaussian excitation beams. This means that CARS confocal microscopy based on Laguerre-Gaussian excitation beams not only can highlight the fine structures of a sample by suppressing the non-resonant CARS signal from bulk water but also has enhanced its ability in revealing the chemical structure information of a sample in comparison with common CARS microscopy based on Gaussian excitation beams. Based on these results, we can conclude that CARS microscopy based on Laguerre-Gaussian excitation beams is much suitable for highlighting the structures with scale comparable to the excitation wavelength. When the size of the structure is much larger or smaller than the excitation wavelength used, the sensitivity of this method decreases.

6. Conclusion

An FDTD method is used to simulate CARS signal generation and propagation for a uniform material and for a tiny spherical scatterer. It has been demonstrated with numerical simulations that, detected CARS signal from a uniform material is very weak when LG01 Laguerre-Gaussian beams are used for the pumping and the Stokes lights, and the CARS signal is collected with a confocal system. On the other hand, when a tiny scatterer with diameter comparable to the excitation wavelength is included in the focal volume, the distribution of the excitation fields and the induced nonlinear polarization are remarkably changed, and the scattering pattern is totally different from that of the uniform bulk material, and the detected CARS signal intensity is stronger than that of a uniform specimen. Thus the fine structures of the specimen are highlighted and the bulk scattering is suppressed. This is a kind of very efficient differential image technique in CARS microscopy. By calculating the CARS signal of scatterers of various diameters, it is found that this method is much suitable for enhancing the structures with a size of the excitation wavelength, while enhancement in CARS signal for structures much larger or smaller than the wavelength used is not very effective. Furthermore, we have demonstrated that the ratio of CARS signal coming from a scatterer with respect to the non-resonant contribution from water inside the focal volume of excitation beams can be high with our proposing differential CARS microscopy technique with LG01 Laguerre-Gaussian excitation beams. This makes the ability of CARS microscopy in retrieving the chemical structural information of the sample to be enhanced compared to that of common CARS microscopy.

Acknowledgments

This work was supported by the Creative Research Initiatives (CRI) Program of Korea Science and Engineering Foundation (KOSEF) / Ministry of Science and Technology (MOST).